

DUSTY STARBURSTS AND THE FORMATION OF ELLIPTICAL GALAXIES: A SCUBA-2 SURVEY OF A $z = 1.46$ CLUSTER*

C.-J. MA¹, IAN SMAIL^{1,2}, A. M. SWINBANK^{1,2}, J. M. SIMPSON¹, A. P. THOMSON¹, C.-C. CHEN¹, A. L. R. DANIELSON², M. HILTON³,
K. TADAKI⁴, J. P. STOTT², AND T. KODAMA^{4,5}

¹ Centre for Extragalactic Astronomy, Department of Physics, Durham University, South Road, Durham DH1 3LE, UK

² Institute for Computational Cosmology, Durham University, South Road, Durham DH1 3LE, UK

³ Astrophysics & Cosmology Research Unit, School of Mathematics, Statistics & Computer Science,
University of KwaZulu-Natal, Private Bag X54001, Durban 4000, South Africa

⁴ National Astronomical Observatory of Japan, Mitaka, Tokyo 181-8588, Japan

⁵ Department of Astronomical Science, The Graduate University for Advanced Studies, Mitaka, Tokyo 181-8588, Japan

Received 2014 October 17; accepted 2015 April 23; published 2015 June 23

ABSTRACT

We report the results of a deep SCUBA-2 850 and 450 μm survey for dust-obscured ultra-/luminous infrared galaxies (U/LIRGs) in the field of the $z = 1.46$ cluster XCS J2215.9–1738. We detect a striking overdensity of submillimeter sources coincident with the core of this cluster: $\sim 3\text{--}4 \times$ higher than expected in a blank field. We use the likely radio and mid-infrared counterparts to show that the bulk of these submillimeter sources have spectroscopic or photometric redshifts that place them in the cluster and that their multiwavelength properties are consistent with this association. The average far-infrared luminosities of these galaxies are $(1.0 \pm 0.1) \times 10^{12} L_{\odot}$, placing them on the U/LIRG boundary. Using the total star formation occurring in the obscured U/LIRG population within the cluster, we show that the resulting mass-normalized star formation rate for this system supports previous claims of a rapid increase in star formation activity in cluster cores out to $z \sim 1.5$, which must be associated with the ongoing formation of the early-type galaxies that reside in massive clusters today.

Key words: galaxies: clusters: individual (XMMXCS J2215.9–1738) – galaxies: evolution – galaxies: formation

1. INTRODUCTION

The relationship between star formation and local galaxy density is one of the clearest pieces of evidence of the effect of environment on galaxy evolution. In the local universe the star formation rate (SFR) of galaxies increases with galaxy density up to the scale of galaxy groups and then drops sharply in the denser environment of clusters (e.g., Lewis et al. 2002; Gómez et al. 2003). As a consequence, galaxy clusters are dominated by passive early types (ellipticals and lenticular galaxies) whose stellar populations indicate little recent star formation activity, while the low-density field is populated by star-forming spiral galaxies (e.g., Dressler et al. 1997; Smith et al. 2005). As all galaxies must have been “star-forming” at some time, this difference suggests that some feature of dense environments has acted to transform star-forming galaxies into the passive populations that dominate these regions today.

However, the fraction of star-forming galaxies (or equally late-type, disk galaxies) in clusters increases rapidly with redshift (e.g., Dressler et al. 1997), which suggests that the environment of growing clusters may have been less hostile in the past. Indeed, mid-infrared and submillimeter wavelength observations have revealed populations of strongly star-forming (ultra-)luminous infrared galaxies (U/LIRGs) in more distant clusters (e.g., Brodwin et al. 2013; Pintos-Castro et al. 2013; Alberts et al. 2014; Santos et al. 2014, 2015; Smail et al. 2014). This enhanced activity means that the mass-normalized integrated SFR for massive clusters evolves rapidly with redshift, $\Sigma(\text{SFR})/M_{\text{cl}} \propto (1+z)^{\alpha}$ with α as high as 7 (e.g., Geach et al. 2006; Popesso et al. 2011, 2012). Below $z \sim 1$, these vigorously star-forming systems are generally

found on the outskirts of clusters and are inferred to be infalling, while the star formation activity is still suppressed at the centers of clusters (e.g., Santos et al. 2013). However, at $z \sim 1.5$ and beyond, strongly star-forming galaxies have been identified in the cluster cores (Hayashi et al. 2010; Tadaki et al. 2012). This has been claimed to represent the “reversal” of the star formation–density relation (e.g., Tran et al. 2010; Santos et al. 2015).

XMMXCS J2215.9–1738 (XCS J2215 hereafter) at $z = 1.46$ is an excellent target to study the nature of star formation activity in a high-redshift cluster. It is one of the most distant clusters discovered in X-rays (Stanford et al. 2006), demonstrating that it represents a deep gravitational potential. A series of extensive multiwavelength follow-up programmes (e.g., Hilton et al. 2007, 2009, 2010) confirm that XCS J2215 is indeed a relatively well developed cluster. Using *XMM-Newton* and *Chandra* observations, Hilton et al. (2010) measured an X-ray luminosity of $L_X = 2.9_{-0.4}^{+0.6} \times 10^{44} \text{ erg s}^{-1}$ and a temperature of $T_X = 4.1_{-0.9}^{+0.6} \text{ keV}$. The velocity dispersion for galaxies within the virial radius ($R_{200} = 0.8 \text{ Mpc}$) is $\sigma_v = 720 \pm 110 \text{ km s}^{-1}$, suggesting that the cluster lies on the self-similar $\sigma_v\text{--}T_X$ scaling relation (Hilton et al. 2010). This then implies a cluster mass of $M_{\text{cl}} \sim 3 \times 10^{14} M_{\odot}$ using the $M_{\text{cl}}\text{--}\sigma_v$ relation (e.g., Koyama et al. 2010). However, the cluster is unlikely to be virialized since it lies below the local $L_X\text{--}T_X$ relation (e.g., Markevitch 1998), and there is also mild bimodality in the velocity distribution of the 44 cluster members identified in Hilton et al. (2010).

XCS J2215 was one of the first clusters in which a reversal in the star formation–density relation was identified. Hayashi et al. (2010) found 12 [O II] emitters within 0.25 Mpc of the cluster center (see also Hayashi et al. 2011, 2014). In addition, Hilton et al. (2010) found two mid-infrared bright, apparently

* *Herschel* is an ESA space observatory with science instruments provided by European-led Principal Investigator consortia and with important participation from NASA.

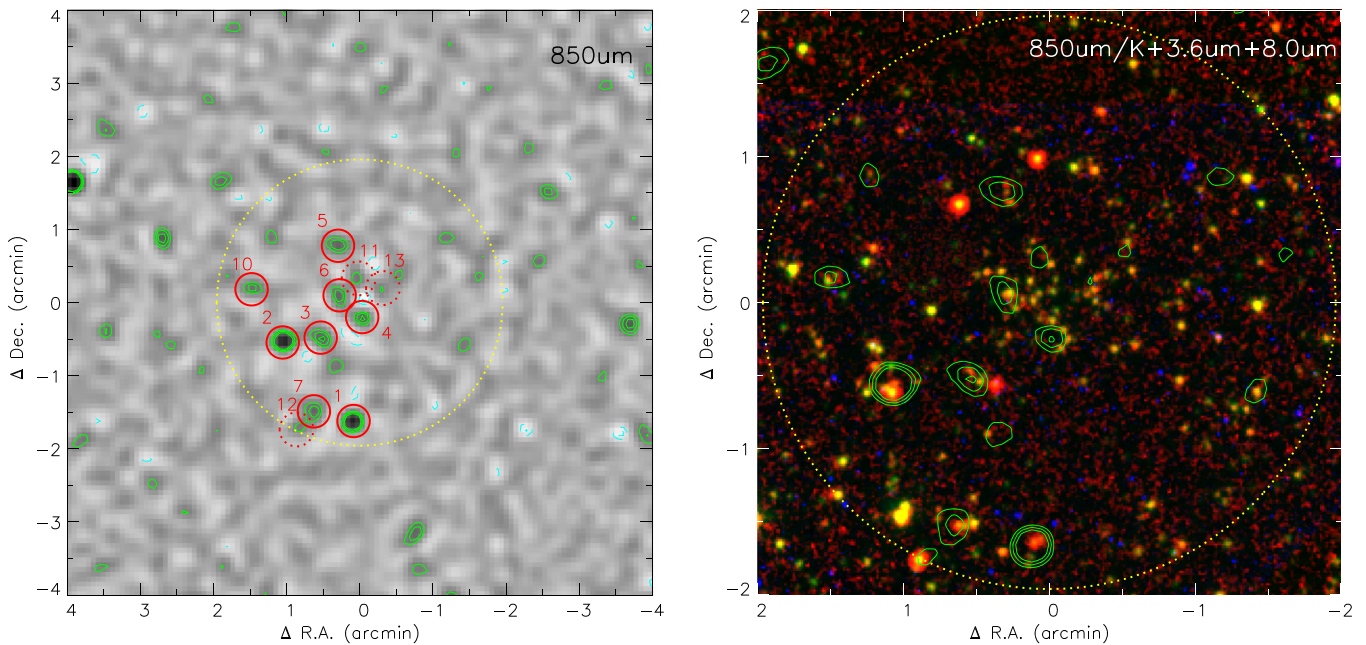


Figure 1. Left: $8' \times 8'$ area around the core XCS J2215 from our $850 \mu\text{m}$ SCUBA-2 map with the detected sources within a 1 Mpc projected radius of the cluster center marked; the red solid circles indicate the 4σ detections at $850 \mu\text{m}$, while the red dashed circles mark the fainter $850 \mu\text{m}$ sources ($>3\sigma$), which are also simultaneously detected in all of the *Herschel* PACS $70 \mu\text{m}$, $160 \mu\text{m}$, and MIPS $24 \mu\text{m}$ bands. We see a strong overdensity of SMGs in the core regions of the cluster, which we associate with a population of ULIRG cluster members. The large dashed yellow circle shows the 1 Mpc radius, and we also plot the 3σ , 4σ , and 5σ positive (green) and negative (cyan) contours of the $850 \mu\text{m}$ map. Right: true-color image of the central 1 Mpc radius region highlighted in the left panel (again shown by the large dashed yellow circle). This is constructed from K_s , $3.6 \mu\text{m}$, and $8 \mu\text{m}$ images, and we overlay the same SCUBA-2 $850 \mu\text{m}$ signal-to-noise contours. Several of the SMGs coincide with galaxies with very red near-infrared colors, much redder than the bulk of the passive cluster galaxies that define the strong overdense population in the cluster core.

star-forming, cluster members within 0.2 Mpc of the center using *Spitzer*/MIPS. These studies suggest that both high- and low-SFR galaxies are found in the densest regions of this cluster, and they showed that the star formation density does not drop at the cluster core. However, at the redshift of XCS J2215 estimating the total SFR from the *Spitzer* MIPS $24 \mu\text{m}$ luminosity is complicated by the presence of both polycyclic aromatic hydrocarbon (PAH) emission and potentially strong silicate absorption features in the band, as well as potential contamination from continuum emission due to active galactic nuclei (AGNs). Similarly, as we demonstrate later in the paper, estimating the total SFRs from $[\text{O II}]$ fluxes also suffers from uncertainties due to the dust obscuration. An independent route to identify strongly star-forming galaxies and determine their SFR is to use the dust thermal emission in the far-infrared and submillimeter wavebands. In this paper, we have therefore combined new SCUBA-2 submillimeter observations of XCS J2215 with archival mid- and far-infrared and radio data to study the SFR and dust properties of the galaxy population in this $z = 1.46$ cluster.

Throughout this paper, we adopt a Λ CDM cosmology with $H_0 = 70 \text{ km s}^{-1} \text{ Mpc}^{-1}$, $\Omega_\Lambda = 0.7$, and $\Omega_m = 0.3$. In this cosmology, $1''$ corresponds to 8.5 kpc at the cluster redshift. The cluster center derived from the X-ray centroid is at $22 15 59.5, -17 38 03$ (J2000) (Hilton et al. 2010). Magnitudes are quoted in the AB system.

2. OBSERVATION AND DATA REDUCTION

This work is primarily based on the submillimeter maps at 450 and $850 \mu\text{m}$ obtained with the Submillimetre Common-User Bolometer Array 2 (SCUBA-2, Holland et al. 2013) on the James Clerk Maxwell Telescope (JCMT). In addition, we

compile multiwavelength images and photometry of the submillimeter galaxies (SMGs) from various archives, including *Spitzer*, *Herschel*,⁶ *Hubble Space Telescope* (*HST*), and the Karl G. Jansky Very Large Array (JVLA). We also collate redshifts and optical/near-infrared data for galaxies in this field from Hilton et al. (2010) (see also Hilton et al. 2007, 2009; Hayashi et al. 2010).

2.1. SCUBA-2 Observations

The SCUBA-2 observations of XCS J2215 are performed in 2013 July–August in Band 1 conditions ($\tau_{225} \leq 0.05$) as part of projects M13AU29 and M13BU10. The simultaneous 450 and $850 \mu\text{m}$ observations yield a total integration of 8 hr, as 12 40-minute scans, centered on the cluster. The data from each scan are processed individually to make maps using the SMURF⁷ reduction software package (Chapin et al. 2013; Jenness et al. 2013). These maps, in units of pW, are calibrated to Jy using the canonical calibration factor of $\text{FCF}_{450} = 491 \pm 67 \text{ Jy beam}^{-1} \text{ pW}^{-1}$ and $\text{FCF}_{850} = 537 \pm 24 \text{ Jy beam}^{-1} \text{ pW}^{-1}$ at 450 and $850 \mu\text{m}$, respectively, which are consistent with the calibration from flux standards obtained on the relevant nights. We co-add the individual exposures using the PICARD package (e.g., Jenness et al. 2008) to construct the final map in each band. Finally, we apply a matched filter to the maps with beam FWHM of $8''$ and $15''$ at 450 and $850 \mu\text{m}$, respectively, to improve the sensitivity for point-source detection. The 1σ noise levels at the center of the final maps are 5.4 and

⁶ *Herschel* is an ESA space observatory with science instruments provided by European-led Principal Investigator consortia and with important participation from NASA.

⁷ <http://starlink.jeo.hawaii.edu/docs/sc21.htx/sc21.html>

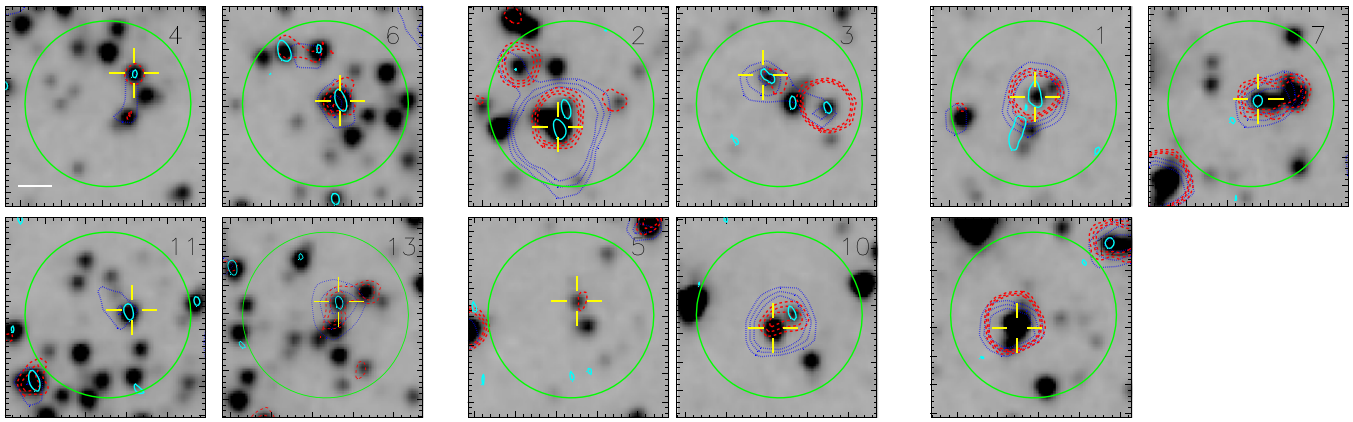


Figure 2. IRAC 3.6 μm images of the 11 850 μm detected SMGs in our sample centered on the positions in Table 1. The images are separated into three groups according to their projected distance to the cluster center: $r_c < 0.25$ Mpc (left), $r_c = 0.25\text{--}0.7$ Mpc (middle), and $r_c = 0.75\text{--}1.0$ Mpc (right). We show the 850 μm beam as a green circle and the identified counterparts with the yellow crosses. We overlay $[3\sigma, 4\sigma, 5\sigma]$ 24 μm contours with a dashed red line, a 4σ contour at 1.4 GHz in cyan, and $[3\sigma, 4\sigma, 5\sigma]$ for PACS 70 μm in solid blue. The most likely counterparts are frequently radio detected and usually correspond to the brightest PACS counterpart in the beam. The major tick marks show $5''$ increments. The white line at the bottom left of the first panel indicates 50 kpc at $z = 1.46$.

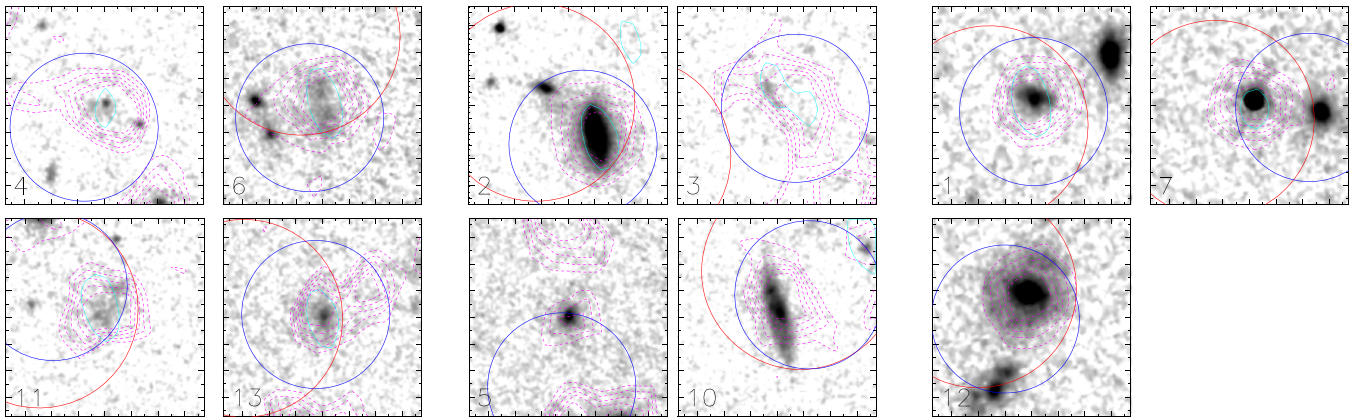


Figure 3. *HST* ACS F814W images of counterparts to 8 of the 850 μm detected SMGs in our sample and WFC3 F160W imaging of the remaining 3 (SMG 01, 07, and 12), separated in terms of radius as in Figure 2. We show the SCUBA-2 450 μm beam as a red circle, the PACS 70 μm as a blue circle, the IRAC 3.6 μm as dashed magenta contours, and the 4σ 1.4 GHz radio contour in cyan. The most likely counterparts from the radio/MIPS-based deblending are consistent with the positions of the 450 μm sources (where present) and are also the brightest 8 μm sources in the error circles, evidence of their very red infrared colors. The ACS images are log-scaled and have been smoothed with a $0''.05$ Gaussian. The major tick marks indicate $1''$ increments.

$0.63 \text{ mJy beam}^{-1}$ at 450 and 850 μm , respectively. The sensitivity drops to 50% at the radius of ~ 5.4 from the map center due to the scan coverage of the DAISY pattern. The central $8' \times 8'$ area of the match-filtered 850 μm image is shown in Figure 1.

To determine the accuracy of the absolute astrometry of the 850 μm map, we compare the coordinates of 850 μm sources (detected at $>3\sigma$) with the closest matched counterparts at 24 μm . After removing three outliers, the mean offset of the 17 counterparts at 24 μm is $\Delta\text{R.A.} = 1''.4 \pm 0''.6$ and $\Delta\text{decl.} = -0''.4 \pm 0''.8$. We correct the astrometry of the 850 μm map using the 24 μm offsets. We similarly confirm that astrometry of the 450 μm map is consistent using the counterparts of sources at 24 μm . The mean offsets are $\Delta\text{R.A.} = -0''.2 \pm 0''.6$ and $\Delta\text{decl.} = 0''.1 \pm 0''.6$. Thus, there is no significant offset identified, and so we choose not to correct the astrometry.

2.2. Radio Observations

We retrieve archival JVLA observations of XCS J2215 (Project 11A-241) taken in *L* band in A-configuration over six nights in 2011 August–September. For these observations the

correlators were configured to give two spectral windows centered at 1.264 and 1.392 GHz, each containing 64 channels with 128 MHz total bandwidth. The total on-source integration time was 15 hr. The amplitude and passband calibrator 3C 48 was observed at the beginning of observation each night, and every two scans of XCS J2215 were bracketed by the 2-minute scans of the phase calibrator J 2246–1206.

We reduce the data using the COMMON ASTRONOMY SOFTWARE APPLICATIONS⁸ (CASA) software (McMullin et al. 2007). One of the two spectral windows (1.264 GHz) suffered from severe radio frequency interference (RFI), and we apply the automatic RFI excision mode “rflag” of the FLAGDATA package in CASA. The data from each spectral window are then calibrated in bandpass, phase, and amplitude using the calibrators, respectively. The combined data from the two spectral windows are used to make a continuum image with robust weighting and a pixel size of $0''.4$. The image is self-calibrated to improve the sensitivity, which reaches a 4σ limit of $\sim 30 \mu\text{Jy beam}^{-1}$ at the center of the final image. The synthesized beam size is $2''.3 \times$

⁸ <http://casa.nrao.edu/>

1''2 (P.A. = 195°). Figures 2 and 3 show the contours of the radio emission over the infrared and optical imaging.

2.3. Archival Observations

To investigate the rest-frame multiwavelength properties of the submillimeter sources seen in the cluster, we have exploited the images and photometry from *HST*, Subaru, and *Spitzer* compiled by Hilton et al. (2010) (see also Dawson et al. 2009; Hilton et al. 2009). We show the Subaru K_s and *Spitzer* IRAC imaging of the cluster in Figure 1 and thumbnails of the *HST* imaging of the individual SMGs in Figure 2.

The details of z_{850} , K_s , IRAC, and MIPS data can be found in Hilton et al. (2009, 2010) and the references therein, but we repeat the essential information here.

HST z_{850} : the observation was performed using Advanced Camera for Surveys (ACS) through the F850LP filter (Dawson et al. 2009) (project ID: 10496). The total exposure time was 16.9 ks, and the 5σ magnitude limit of the catalog in Hilton et al. (2009) is $z_{850} \sim 26.0$. We retrieved the ACS images of the cluster from the *HST* archive,⁹ as well as a 0.7 ks WFC3 F160W near-infrared image (project ID: 12990). These images provide ~ 1 kpc resolution imaging of the cluster members at rest-frame wavelengths approximately corresponding to the *U* and *R* bands. These images are displayed in Figure 3 to illustrate the rest-frame UV–optical morphologies of the SMGs.

Subaru K_s : the observation was performed using the MOIRCS instrument (Hilton et al. 2009). The total integration time is 1.24 ks, and the 5σ magnitude limit is $K_s \sim 24.3$.

Spitzer IRAC and MIPS: a total of 1500 s integration was obtained with IRAC (Program 50333) and 1800 s with MIPS. The IRAC photometry was measured with a 4'' diameter circular aperture with aperture correction measured by Barmby et al. (2008). We use the IRAC source catalog compiled in Hilton et al. (2010), of which sources are cross-matched against their K_s -band catalog to find the nearest match within 1''2 radius. Our 24 μm catalog also comes from Hilton et al. (2010) and contains 152 sources detected at $>5\sigma$, of which eight are associated with cluster members (four spectroscopically confirmed and four selected using photometric redshifts). The 50% completeness limit of the catalog is $\sim 70 \mu\text{Jy}$ (Hilton et al. 2010), corresponding to a limit of $L_{\text{IR}} > 3 \times 10^{11} L_{\odot}$ at the cluster redshift using templates from Dale & Helou (2002) or an SFR of $>60 M_{\odot} \text{yr}^{-1}$ based on Kennicutt (1998).

In addition to the data described above, we also obtain longer-wavelength archival observations of the cluster taken with the PACS instrument on *Herschel* at 70 and 160 μm . The two observations are performed under an open time OT1 program (see Santos et al. 2013) on 2012 April 30 (Obsid: 1342245177) and 2012 December 19 (Obsid: 1342257511) and are retrieved from the *Herschel* Science Archive. We process the data using the standard procedures with HIPE software (build: 11.0.2938; Ott 2010; see Lutz et al. 2011 for more details). We then use the SOURCEEXTRACTORDAOPHOT routines in the package of HIPE (Ott 2010) to detect sources, and we measure their photometry in 4''2 and 8''5 radius apertures at 70 and 160 μm , respectively. The sky background is measured in an annulus between 20'' and 30'', and an automatic aperture correction from SOURCEEXTRACTORDAOPHOT is applied.

The 1σ noise in these images is 0.4 and 1.4 mJy at 70 and 160 μm , respectively, measured using random aperture photometry in regions free from sources. In the central 2' area of the maps, we detect 23 and 14 sources at 70 and 160 μm , respectively, above a 3σ limit. Following the discussion of astrometry in Section 2.1, we confirm that the mean offset of sources in the 70 μm map is insignificant ($\Delta\text{R.A.} = -0''1 \pm 1''0$ and $\Delta\text{decl.} = 0''5 \pm 1''3$) using the counterparts of sources at 24 μm .

2.4. Cluster Galaxy Catalog and Redshift Measurements

In our analysis we use the catalog of cluster galaxies compiled in Hilton et al. (2009) and Hayashi et al. (2014) (see also Hilton et al. 2007, 2010; Hayashi et al. 2010, 2011). Again, we only summarize the most relevant results here.

The sample in Hilton et al. (2009) includes 64 member galaxies: 24 of them are spectroscopically confirmed, and the remainder are selected by photometric redshifts. The photometric redshifts (z_p) are calculated with the i_{775} , z_{850} , J , and K_s photometry. The uncertainty in the photometric redshifts, $\delta z = (z_s - z_p)/(1 + z_s)$, of the 36 galaxies with spectroscopic redshifts at $z_s > 1.0$ is $\sigma_{\delta z} = 0.039$. The cluster members are selected by, first, requiring that their photometric redshift lies in $z_p = 1.27\text{--}1.65$ (i.e., z_p falls within the $2\sigma_{\delta z}$ of the cluster redshift, $z = 1.46$) and, second, applying a quality cut on the photometric redshift such that $p_{\Delta z} > 0.9$ (see Hilton et al. 2009). Using these two criteria, of the spectroscopically confirmed non-members, only two would be misclassified as members based on their photometric redshifts, i.e., $\sim 5\%$ of photometric redshift members may be non-members of the spectroscopic sample. In addition, 4 of the 24 spectroscopically confirmed cluster members with $z_s = 1.445\text{--}1.475$ are missed by the photometric redshift selection corresponding to $\sim 80\%$ completeness.

Hayashi et al. (2014) present a narrowband survey to search for [O II] emitters in and around XCS J2215 using two filters (NB912 and NB921) with Suprime-cam on Subaru. The sample includes 170 [O II] emitters at $z \sim 1.46$ with a redshift accuracy of $\sigma((z - z_s)/(1 + z_s)) = 0.002$. The central wavelength and FWHM of the NB912 (NB921) filters are 9139 (9196) Å and 134 (132) Å, equivalent to a velocity difference of $\sim 2000 \text{ km s}^{-1}$ or a redshift range of $\delta z = \pm 0.02$ at $z = 1.46$. To exclude the contamination of H α or [O III] emissions at higher redshifts, they have applied a BzK color selection illustrated in Hayashi et al. (2010). The 5σ limiting magnitudes of the narrowband filter observations are 25.2 and 25.4, respectively, corresponding to SFRs of 2.6 and $2.2 M_{\odot} \text{yr}^{-1}$ according to the relation of Kennicutt (1998).

3. SUBMILLIMETER SOURCE DETECTIONS

In the SCUBA-2 850 μm map (Figure 1), we detect 16 sources above 4σ significance within the region with $>50\%$ sensitivity, i.e., the radius of $\sim 5'.4$ from the map center. The 4σ significance cut corresponds to a flux limit of ~ 2.6 mJy at the map center. The reported fluxes are not statistically de-boosted, but we derive deblended fluxes for these below. Eight of these 16 sources are located within 1 Mpc of the cluster center (1'.95 radius), where the 1σ noise at 850 μm is in the range of 0.63–0.80 mJy beam $^{-1}$. To estimate the false detection rate, we search for negative “sources” in the map and confirm that there are no negative “sources” with signal-to-noise ratio (S/N) < -4 in this area.

⁹ <http://archive.stsci.edu/>

Table 1
Properties of the 850 μm Sources within 1 Mpc Radius of XCS J2215

ID	R.A. (J2000)	Decl. (J2000)	f_{850} (mJy)	f_{450} (mJy)	f_{160} (mJy)	f_{70} (mJy)	f_{24} (mJy)	$f_{1.4}$ (μJy)	r_c (Mpc)	P_{24}	$P_{1.4}$
04	22 15 58.4	-17 38 19	3.2 ± 0.6	<16	8.1 ± 1.4	1.0 ± 0.4	0.17 ± 0.01	33 ± 8	0.15	0.13	0.05
06	22 15 59.8	-17 37 59	2.9 ± 0.6	16 ± 5	8.6 ± 1.4	1.3 ± 0.4	0.22 ± 0.01	76 ± 8	0.07	0.03	0.01
11	22 15 58.7	-17 37 47	2.2 ± 0.6	18 ± 5	9 ± 4	1.5 ± 0.5	0.09 ± 0.01	86 ± 8	0.16	0.02	0.01
13	22 15 57.3	-17 37 55	1.9 ± 0.6	16 ± 5	10.0 ± 1.4	2.2 ± 0.4	0.22 ± 0.01	52 ± 9	0.24	0.03	0.01
02	22 16 02.9	-17 38 35	5.9 ± 0.7	21 ± 6	19.4 ± 1.4	7.8 ± 0.4	0.72 ± 0.01	63 ± 9	0.55	0.05	0.02
03	22 16 00.6	-17 38 35	3.4 ± 0.7	17 ± 6	7.5 ± 1.4	1.7 ± 0.4	0.23 ± 0.01	66 ± 9	0.32	0.07	0.04
05	22 15 59.8	-17 37 19	3.1 ± 0.7	<17	<4	<1.3	0.20 ± 0.01	<25	0.39	0.01	...
10	22 16 04.8	-17 37 51	3.0 ± 0.8	24 ± 6	10.6 ± 1.3	2.2 ± 0.5	0.28 ± 0.01	53 ± 8	0.69	0.04	0.01
01	22 15 59.0	-17 39 43	6.6 ± 0.8	26 ± 6	10.5 ± 1.5	2.8 ± 0.4	0.56 ± 0.01	168 ± 10	0.84	0.01	0.003
07	22 16 01.2	-17 39 35	3.5 ± 0.8	21 ± 7	10.0 ± 1.4	1.6 ± 0.5	0.46 ± 0.01	47 ± 10	0.82	0.000	0.000
12	22 16 02.0	-17 39 47	2.7 ± 0.8	22 ± 7	8.4 ± 1.5	3.1 ± 0.4	1.30 ± 0.01	<29	0.98	0.05	...

Note. The columns list the ID, the 850 μm position, and fluxes at 850 and 450 μm measured using SCUBA-2, with PACS on *Herschel* at 160 and 70 μm , with MIPS on *Spitzer* at 24 μm , and with JVLA at 1.4 GHz. For non-detections with $S/N < 3$, the 3σ upper limit is listed. The next column gives the cluster-centric radius of each source in Mpc. The 850 μm sources all have close and bright 1.4 GHz and/or 24 μm counterparts, and the final two columns are the P -statistics of these counterparts at 24 μm and 1.4 GHz. The sources are grouped in the table according to the projected distance from the cluster core (r_c). Within each group, the sources are ranked according to their 850 μm fluxes.

Using the number counts of the 870 μm sources in the Extended *Chandra* Deep Field South from Karim et al. (2013), we derive the density of submillimeter sources with a flux limit of ~ 2.6 mJy and estimate that the expected number in a typical field is ~ 2 within the same projected area. Thus, the central regions of the XCS J2215 map display a $\sim 3\text{--}4 \times$ overdensity in terms of submillimeter sources.

In addition, there are eight fainter 850 μm sources with $S/N = 3\text{--}4$ in the central 1 Mpc area. Since many of these modest-significance sources may be spurious, we use the data at 450, 160, and 70 μm to verify the detections and find that three of the eight are also simultaneously detected with $S/N > 3$ at all three of the shorter wavelengths. This detection fraction is consistent with a simple test of the false detection rate of faint 850 μm sources from searching for negative “sources” in the map, which indicates a false detection rate of about 70% for sources with $S/N = 3\text{--}4$. We also verify that none of these negative “sources” are detected at $S/N > 3$ in all three of the shorter-wavelength bands, which suggests that the three faint 850 μm sources with $S/N = 3\text{--}4$ that are detected in MIPS/PACS are likely to be real. Therefore, we include these three sources (SMG 11, 12, and 13) in the final catalog and discard the other five.

To summarize, we list the fluxes from mid-infrared to radio of the 11 sources in Table 1, and we show the IRAC 3.6 μm thumbnails of each in Figure 2. The IDs of the sources are numbered in descending order of 850 μm S/N .

4. COUNTERPART IDENTIFICATIONS

To precisely locate the submillimeter sources, we first use both the high-resolution 24 μm and 1.4 GHz images to identify their counterparts, and then we match these to sources in the optical and near-infrared data. Next, we use the redshift catalog of Hilton et al. (2010) and the [O II] emitter sample of Hayashi et al. (2014) to determine whether the counterparts are likely cluster members.

As shown in Figure 2, all 11 of the 850 μm sources have possible counterparts at 24 μm . Indeed, many of them have multiple candidates within the 850 μm SCUBA-2 beam

(Figure 2). At 1.4 GHz, we find unique counterparts above the 4σ radio flux limit ($\sim 30 \mu\text{Jy}$) in the beam of six 850 μm sources and multiple counterparts in the three sources SMG 01, 02, and 03.

To determine the statistical significance of these potential counterparts, we calculate the standard corrected Poissonian probability of a positional match (P ; Downes et al. 1986). In Table 1, we list the counterpart probabilities calculated from the 1.4 GHz and 24 μm catalogs. The probabilities for all the proposed 1.4 GHz identifications are $P_{1.4} \leq 0.05$ (normally taken to signify a robust identification), and for those without 1.4 GHz identifications, the probabilities derived for the 24 μm counterparts are also $P_{24} \leq 0.05$ (fortunately, the two 850 μm sources that lack 1.4 GHz counterparts, SMG 05 and SMG 12, are associated with single 24 μm counterparts). Thus, for all 11 of the SMGs we identify single, robust counterparts at 1.4 GHz and/or 24 μm to the 850 μm sources. The higher-resolution PACS 70 μm and SCUBA-2 450 μm imaging also provides an alternative route to test these identifications, and we show the PACS map in Figure 2 and the 70 and 450 μm beams in Figure 3, confirming the likely counterparts.

4.1. Multiplicity and 850 μm Flux Deblending

Recent ALMA follow-up of submillimeter sources taken from single-dish blank-field surveys has shown that they frequently contain multiple submillimeter sources when mapped at high spatial resolution (Hodge et al. 2013; Simpson et al. 2015). Indeed, Hodge et al. (2013) demonstrate that robust counterparts (those with $P \leq 0.05$) identified through radio and mid-infrared emission, as we have done here, are correct in 80% of cases, but they are also incomplete, recovering only 45% of the counterparts. This suggests that our identifications are likely to have reasonable purity, as indicated by their correspondence with the 70 and 450 μm positions. As we see later, the fact that many of these counterparts appear to be cluster members at $z = 1.46$ may also explain the high recovery rate of robust counterparts. This most likely reflects the lower mean redshift of these SMGs, $z \sim 1.5$, compared to the bulk of the field SMG population, $z \sim 2.5$

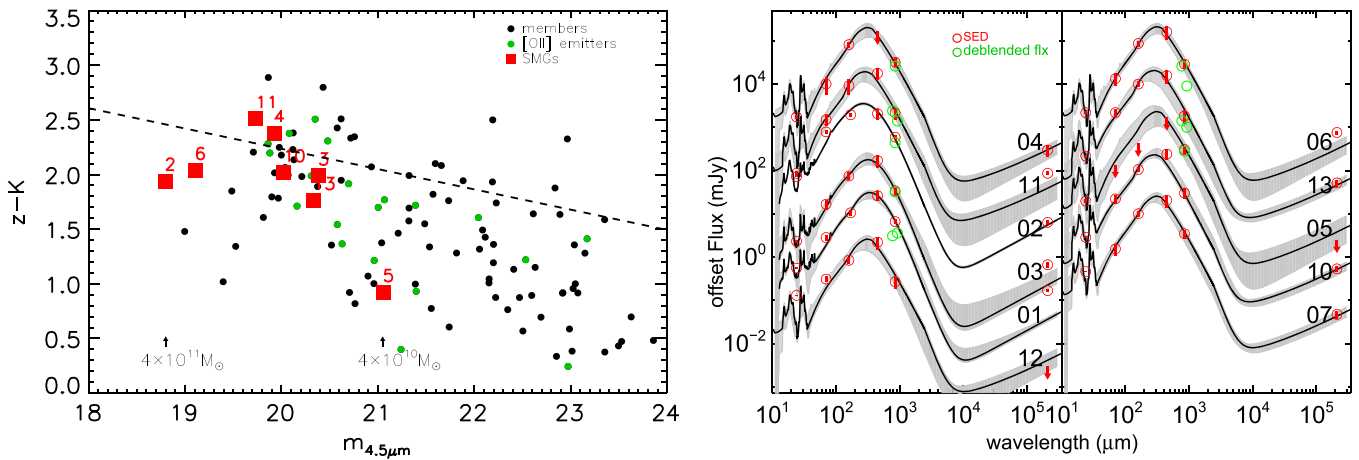


Figure 4. Left: $(z' - K) - m_{4.5\mu\text{m}}$ color–magnitude diagram for cluster members (roughly corresponding to rest-frame $(U - I) - M_H$). We plot the SMGs, the [O II] narrowband emitters from Hayashi et al. (2010, 2014), and the photometric redshift members from Hilton et al. (2010). The dashed line is the red sequence derived using the early-type cluster members in Hilton et al. (2009). This demonstrates that the SMGs are among the reddest cluster galaxies, likely due to strong dust obscuration, and are also among the most luminous in the rest-frame H band, suggesting that they have high stellar mass. Similar behavior has been seen in SMG members of other high-redshift clusters (e.g., Smail et al. 2014). For reference, the stellar masses of SMG 02 and SMG 05 calculated based on $m_{4.5\mu\text{m}}$ are noted in the bottom. Right: infrared to radio SED of the SMG counterparts. The fluxes are plotted as red circles with 1σ errors, and the non-detections are shown by 3σ limits; we also show the deblended fluxes for the sources in green (see Section 5.1). The SED fit (solid line) excludes the $24\mu\text{m}$, and the redshifts are fixed to the cluster redshift in all cases. The gray area shows the 1σ confidence range of the fit. The majority of the SMGs have SEDs that are well fit by the template libraries at the cluster redshift, showing that the dust emission from these galaxies is consistent with them being cluster members.

(Simpson et al. 2014), which yields a more advantageous K -correction in the MIPS and radio bands and hence a higher recovery fraction.

Figure 2 also shows potential evidence of multiplicity, with a number of SMGs appearing to have multiple counterparts. In the absence of submillimeter interferometric fluxes for these sources, we have estimated the submillimeter flux for each counterpart by deblending the $850\mu\text{m}$ map using the method in Swinbank et al. (2014) using a position prior including all 1.4 GHz and $24\mu\text{m}$ sources. We plot the fluxes of the individual counterparts (excluding any sources that are undetected based on the deblended fluxes), along with the spectral energy distributions (SEDs) of the sources, in Figure 4. The fluxes of most submillimeter sources are dominated by the counterpart selected by our probabilistic analysis, and their deblended fluxes are not significantly lower than the integrated fluxes. The only exceptions are SMG 02 and SMG 01. For SMG 02, the deblended flux of the major counterpart is ~ 2 mJy lower than the single-dish flux of $S_{850} = 5.9 \pm 0.7$ mJy. For SMG 01, the two possible counterparts share the integrated $850\mu\text{m}$ flux evenly and correspond to two ~ 3 mJy SMGs.

4.2. Cluster Membership

Next, we match the radio and mid-infrared counterparts to the SMGs with the galaxies detected in the IRAC $3.6\mu\text{m}$ image and the photometric and spectroscopic redshift information that we have associated with these galaxies. Many of the matched galaxies are cluster members based on spectroscopic redshifts (SMG 06, 13: Hilton et al. 2010), [O II] emission at the cluster redshift (SMG 03, 04, 11: Hayashi et al. 2010, 2014), or photometric redshifts (SMG 02, 05: Hilton et al. 2010). We tabulate the resulting redshift information in Table 2. We note that all of the SMG counterparts within a 0.8 Mpc radius of the cluster center appear to be cluster members based on either spectroscopic or photometric redshifts (Hilton et al. 2010), or narrowband [O II] emission (Hayashi et al. 2010, 2014). This suggests that gravitational lensing is not a significant factor in

the SMG overdensity observed in the cluster core. However, we have no redshift estimates for the most likely counterparts of the three outermost $850\mu\text{m}$ sources, SMG 01, SMG 07, and SMG 12.

As we have noted, ALMA has demonstrated the need for robust submillimeter identifications to reliably associate potential SMG counterparts with submillimeter sources. This is particularly true in crowded fields such as the cluster studied here, given the density of potential counterparts, especially at $24\mu\text{m}$. Nevertheless (in the absence of lensing), the strong overdensity of submillimeter sources around XCS J2215 would suggest a relatively low contamination rate (only two field SMGs are expected in this area), and as we show in Section 5.1, the SEDs of most of these counterparts are consistent with those expected for ULIRGs at the cluster redshift, and so we suggest that the majority of identifications are likely to be correct.

5. ANALYSIS AND DISCUSSION

5.1. Spectral Energy Distributions

In Figure 4 we show the $(z' - K) - m_{4.5\mu\text{m}}$ color–magnitude diagram for the cluster members, including the SMG counterparts, [O II]-detected members from Hayashi et al. (2010, 2014), and K -band members selected using photometric redshifts from Hilton et al. (2010). As seen in previous studies of SMG members of high-redshift clusters (e.g., Smail et al. 2014) and indeed the field SMG population (e.g., Simpson et al. 2014), the SMG counterparts tend to be both redder and more luminous than average field galaxies. This is consistent with their identification as massive, dusty starbursts, where the dust extinction results in red UV–optical colors and the combination of high mass and significant recent star formation means that they are luminous sources in the rest-frame near-infrared. We note that one counterpart, that for SMG 05, appears fainter and bluer than the rest, properties more consistent with the “normal” cluster population on the

Table 2
Derived Properties for the 850 μm Sources in XCS J2215

ID	R.A. (J2000)	Decl. (J2000)	z	L_{IR} ($10^{11}L_{\odot}$)	T_d (K)	SFR _{FIR}	SFR _[O II] ($M_{\odot} \text{ yr}^{-1}$)	SFR _{24μm}	$m_{4.5 \mu\text{m}}$ (AB)	$(z' - K)$ (AB)	Notes
04	22 15 58.10	-17 38 14.1	[O II]	$7.5^{+1.6}_{-2.5}$	28 ± 1 [23]	130^{+30}_{-40}	8	170	19.9	2.38	...
06	22 15 59.64	-17 37 59.0	1.469	$8.0^{+1.4}_{-1.7}$	29 ± 1 [23]	140^{+20}_{-30}	8	240	19.1	2.04	H10:744/747
11	22 15 58.44	-17 37 46.6	[O II]	$8.3^{+2.1}_{-2.9}$	31 ± 3 [24]	140^{+40}_{-50}	11	110	19.7	2.51	...
13	22 15 57.17	-17 37 52.9	1.454	$8.6^{+2.1}_{-1.5}$	32 ± 2 [24]	160^{+30}_{-30}	11	160	20.3	1.76	H10:35
02	22 16 03.07	-17 38 40.0	phot- z	$21.2^{+1.5}_{-2.0}$	29 ± 1 [27]	360^{+30}_{-20}	...	650	18.8	1.94	H10:1022
03	22 16 00.87	-17 38 30.8	[O II]	$8.3^{+1.7}_{-1.7}$	28 ± 1 [22]	130^{+30}_{-30}	10	160	20.4	1.99	H10:983
05	22 15 59.75	-17 37 17.2	phot- z	$10.6^{+4.1}_{-5.8}$	26 ± 2 [23]	150^{+250}_{-80}	...	140	21.1	0.92	Only 850 μm in FIR
10	22 16 04.92	-17 37 54.1	phot- z	$10.2^{+1.7}_{-2.0}$	29 ± 1 [24]	180^{+200}_{-150}	...	220	20.0	2.02	H10:709
01	22 15 58.95	-17 39 42.3	...	$10.9^{+3.0}_{-1.5}$	25 ± 1 [21]	180^{+80}_{-20}	...	510	Radio-bright AGN
07	22 16 01.13	-17 39 34.9	...	$9.4^{+1.9}_{-1.6}$	29 ± 2 [23]	160^{+30}_{-30}	...	380	X-ray AGN
12	22 16 02.27	-17 39 50.1	...	$9.6^{+2.1}_{-1.9}$	29 ± 2 [23]	160^{+30}_{-30}	...	1200	X-ray AGN

Note. The columns list the ID, the F814W position of the proposed counterpart, the redshift or source of the membership, the far-infrared luminosity and dust temperature, the star formation rate, the 4.5 μm IRAC magnitude and $(z' - K)$ color, and finally notes on each candidate SMG. In addition to the SFR calculated using the far-infrared SED in this paper, the two SFRs calculated using the flux of [O II] (Hayashi et al. 2010, 2014) and 24 μm are listed for comparison. The SFR counterparts in Hilton et al. (2010) are indicated by H10 and their IDs. In the column listing T_d , the second value (in square brackets) corresponds to the dust temperature derived by taking the wavelength of the peak of the best-fitting dust SED template and assuming $\lambda_{\text{peak}} T_d = 2.897 \times 10^3 \text{ m K}$.

red sequence. This source is also unique in being undetected in all bands from 70 μm to 1.4 GHz, except at 850 μm .

For the galaxies in Figure 4 we can estimate the typical rest-frame H -band absolute magnitudes, which are a crude tracer of their stellar masses, by converting their observed 4.5 μm (which samples close to rest-frame H band) using a model SED based on the reddened burst SED fit from Simpson et al. (2014). This predicts a combined K -correction and distance modulus value of -44.9 , which when applied to the observed 4.5 μm magnitudes gives a median rest-frame H -band absolute magnitude for the SMG sample of $M_H = -25.0 \pm 0.3$. This is marginally brighter than the $M_H = -24.6 \pm 0.2$ derived for IRAC-detected “field” SMGs by Simpson et al. (2014) (see also Hainline et al. 2011), even though the latter typically lie at higher redshifts. The simplest interpretation of this comparison is that the cluster SMGs we find in XCS J2215 may be marginally more massive than comparably star-forming sources in the field.

We note that there are three sources that lie outside the coverage of the HST z_{850} image and so are missing from Figure 4 and the calculation above. However, all three appear to be AGNs: the counterparts to SMG 07 and 12 in Figure 2 are both bright point-like components, and both of these counterparts are X-ray detected (Hilton et al. 2010), suggesting that these two SMGs host unobscured AGNs (which will contaminate their H -band luminosities). In addition, SMG 01 appears to have a strong radio excess over that expected for the best-fit template SED in Figure 4 (see Section 5.1.4), also suggesting an AGN component. Thus, intriguingly, all three SMGs on the outskirts of the cluster host AGNs.

5.1.1. Template Fitting

To derive the far-infrared luminosity and SFRs of the 850 μm detected cluster members, we follow the procedure in Swinbank et al. (2014) and fit their SEDs using a library of

galaxy templates from Chary & Elbaz (2001), Draine et al. (2007), and Rieke et al. (2009). The fitting is performed with the photometry from far-infrared to 1.4 GHz, but excluding the 24 μm band to avoid the complexity caused by the redshifted PAH and silicate features at the cluster redshift. The redshifts used in the fitting procedure are fixed at the cluster redshift for all sources. The results of this are shown in Figure 4 and Table 2. As Figure 4 shows, the template libraries provide adequate fits to the majority of the SMGs, indicating that their SEDs can be well described by standard templates at the cluster redshift. The median of χ^2 per degrees of freedom (dof) is 0.66, and the values are less than 1 for all sources except for SMG 01 ($\chi^2/\text{dof} = 1.8$), SMG 02 ($\chi^2/\text{dof} = 1.6$), and SMG 12 ($\chi^2/\text{dof} = 2.8$). If we allow the redshift for the sources without spectroscopic redshift to be a free parameter in the fits, the best-fit redshifts are still located within the range of $z = 1.3 - 1.7$, close to the cluster redshift. For all sources without precise redshifts the fits with unconstrained redshifts are not significantly better, $\delta\chi^2 < 0.2$, than those fixed at the cluster redshift.

We note that the fitting of SMG 05, which was already highlighted above, is much more weakly constrained as it is based on a single detection at 850 μm and limits. The best-fit template of SMG 05 predicts fluxes above the detection limits at 70, 160, and 450 μm and 1.4 GHz. This may imply that this source is in fact a higher-redshift field SMG that is not related to the identified cluster counterpart. The presence of a field source within the sample would be consistent with the predicted field contamination, but we note that our subsequent analysis of the integrated SFR in the cluster does not change significantly if this source is included or excluded. Similarly, the other three galaxies without precise redshifts (SMG 01, 07, and 12) are all located outside of $R_{200} \sim 0.8 \text{ Mpc}$ and so are not included in our estimate of the integrated SFR within the virial radius of the cluster derived below. As a result, the

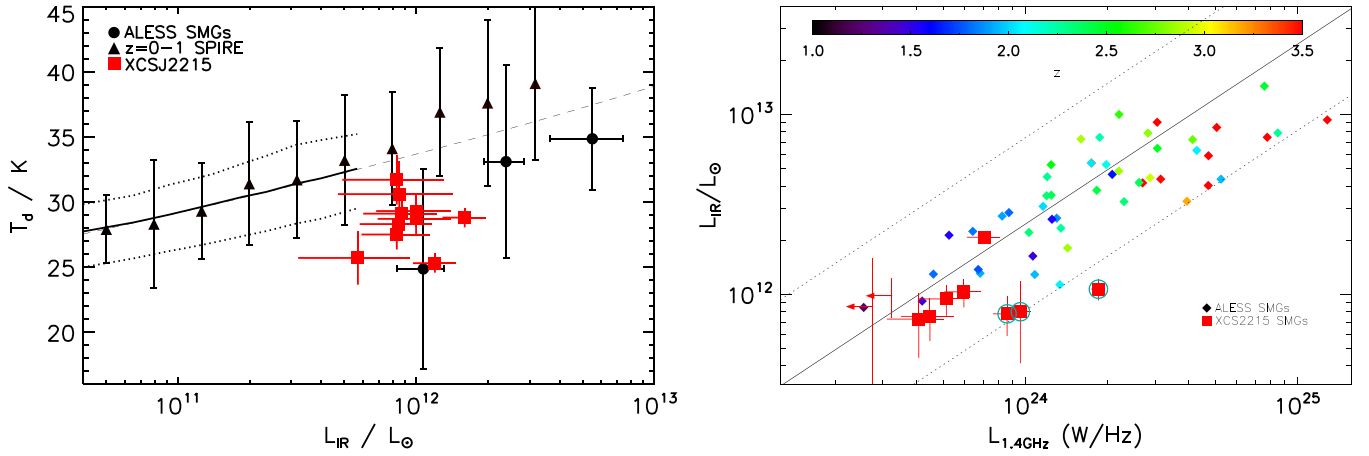


Figure 5. Left: dust temperature and infrared luminosity of the SMGs within 1 Mpc radius of XCS J2215 compared to low-redshift ULIRGs and high-redshift SMGs. We include in the plot the L_{IR} - T_d correlation derived for local $60 \mu\text{m}$ selected *IRAS* galaxies by Chapman et al. (2003); solid line, with 1σ dispersion shown by the dotted line; see also Chapin et al. 2009). This plot shows that at a fixed L_{IR} , the SMGs in XCS J2215 are ~ 5 K cooler than the average temperature of SPIRE-selected U/LIRGs at $z < 1$ (Symeonidis et al. 2013), and also ~ 3 – 4 K hotter than the median temperature of ALMA-identified SMGs with $z > 1.5$ in the Extended *Chandra* Deep Field South (ALESS; Swinbank et al. 2014). This trend is consistent with a decline with redshift of the dust temperature at a fixed luminosity, suggestive of less compact starbursts at higher redshifts. Note that the uncertainties may be underestimated; see Section 5.1 for details. Right: far-infrared–radio correlation for the XCS J2215 SMGs compared to the ALMA-identified SMGs from the ALESS survey (Thomson et al. 2014). We only plot those ALESS SMGs detected at 1.4 GHz in Thomson et al. (2014), and they are color-coded according to their redshifts. The solid line shows the correlation from Ivison et al. (2010) with logarithmic infrared to radio flux ratio $q_{IR} = 2.40$, and the dotted lines represent the $2\sigma_q = \pm 0.48$ range. The three XCS J2215 sources (SMG 01, 06, and 11) with excess radio power in Figure 4 are the three circled points. The ratio of far-infrared to radio luminosities in the XCS J2215 sample is comparable to that seen in the radio-detected ALESS population at similar redshifts.

uncertainties over both their membership and the AGN contribution to their far-infrared luminosities (see Section 5.1) do not affect our discussion.

5.1.2. Infrared Luminosity and Dust Temperature

Using the best-fit models for each SED, we calculate the infrared luminosity L_{IR} in the wavelength range from 8 to $1000 \mu\text{m}$, and the SFR from the relation in Kennicutt (1998) assuming a Salpeter initial mass function. The results are listed in Table 2. To compare the dust temperature in these cluster galaxies with other SMGs, we also estimate the dust temperature (T_d) by fitting the fluxes from 160 to $850 \mu\text{m}$ using a graybody model assuming a dust emissivity of $\beta = 1.5$ and the redshifts in Table 2. We note that it is likely that the uncertainties on the derived temperature are underestimated as we have adopted both fixed redshifts and β in the fitting.

We show the distribution of L_{IR} and T_d for the cluster SMGs in the left panel of Figure 5, where we compare it to both the L_{IR} - T_d trends seen in samples of low-redshift ($z \sim 0.4$) ULIRGs from Symeonidis et al. (2013) and the median values for high-redshift field SMGs from Swinbank et al. (2014). At the typical luminosities of the SMGs in XCS 2215, $L_{IR} \sim 1 \times 10^{12} L_{\odot}$, the SMGs appear to have temperatures that are ~ 3 – 4 K cooler than comparable luminous low-redshift ULIRGs (~ 29 K vs. ~ 34 K, respectively). At these luminosities the ALMA-identified field SMGs from Swinbank et al. (2014), which typically lie at higher redshifts $z \sim 2$ – 3 , are even cooler (~ 25 K). This suggests that the characteristic dust temperature of ULIRGs may decline with increasing redshift, perhaps indicating a more extended distribution of dust in SMGs, compared to local ULIRGs, although the influence of the $850 \mu\text{m}$ sample selection complicates the interpretation of this trend. A number of other studies have suggested similar trends of more extended dust and star formation distributions in SMGs, using a variety of observations (e.g., Chapman

et al. 2003; Hainline et al. 2009; Menendez-Delmestre et al. 2009; Ivison et al. 2010; Swinbank et al. 2014).

5.1.3. Different Measurements of SFRs

We compare the different tracers of star formation in the XCS J2215 galaxies in Table 2. Here we list the SFR calculated from the $[\text{O II}]$ narrowband fluxes (Hayashi et al. 2010, 2014) and $24 \mu\text{m}$ (Hilton et al. 2010) for comparison to the far-infrared. The $\text{SFR}_{[\text{O II}]}$ of those SMGs detected as $[\text{O II}]$ emitters is calculated according to the relation of Kennicutt (1998), which significantly underestimates the SFR of these dust-rich SMGs. An extra attenuation factor of ~ 3 mag at 3727 \AA is required to bring the $\text{SFR}_{[\text{O II}]}$ up to their SFR_{FIR} . In addition, the non-detection of $[\text{O II}]$ emission from the other SMGs suggests an attenuation factor of > 4 mag. To compare the $24 \mu\text{m}$ and far-infrared, we use the tabulated $\text{SFR}_{24 \mu\text{m}}$ for SMG 06 and 13 derived from the Chary & Elbaz (2001) spectral templates by Hilton et al. (2010) to calibrate the SFR of the other SMGs from their $24 \mu\text{m}$ fluxes. As expected for the dusty SMGs, we find that $\text{SFR}_{24 \mu\text{m}}$ is not as biased as the $\text{SFR}_{[\text{O II}]}$, although there are obvious biases associated with mid-infrared-bright AGNs in the sample, and overall the large variation relative to the SFR_{FIR} may be explained by the contamination of PAH features.

5.1.4. Radio Power

The right panel of Figure 5 compares the ratio of far-infrared and radio luminosities for the candidate $z = 1.46$ cluster SMGs to those of a sample of radio-detected, ALMA-identified field SMGs drawn from Thomson et al. (2014). We restrict ourselves to the radio-detected field sample to mimic the requirement for radio identifications of counterparts in XCS J2215. For the XCS J2215 SMGs the radio power density at rest-frame 1.4 GHz is calculated assuming a spectral index of $\alpha = -0.8$. We also plot the far-infrared–radio correlation from

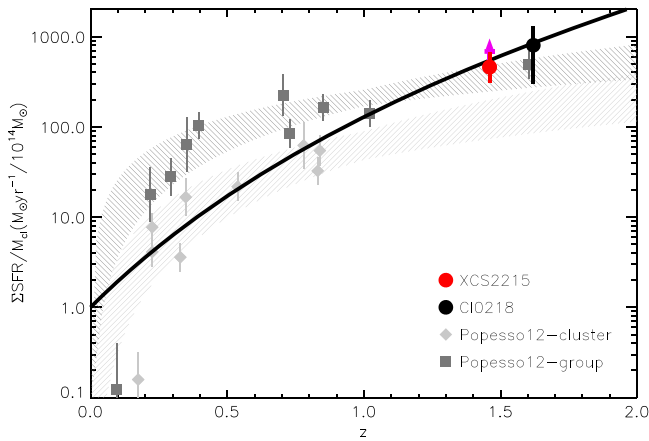


Figure 6. Integrated SFR of clusters and groups normalized by their total mass. We plot the total SFR of XCS J2215 derived from the $850\ \mu\text{m}$ selected SMGs within the virial radius of the cluster. Including the star formation in the $24\ \mu\text{m}$ sources detected in Hilton et al. (2010) and $[\text{O II}]$ emitters detected in Hayashi et al. (2010, 2014), the normalized integrated SFR will increase by a factor of 1.5 and 2.1, respectively, as indicated by the cross and arrow. Compared to the trend of galaxy groups/poor clusters or clusters proposed by Popesso et al. (2011), the mass-normalized SFRs of both XCS J2215 and CI J0218 (Smail et al. 2014) suggest more star formation activity in high-redshift clusters, closer to the power-law evolution proposed by Geach et al. (2006).

Iverson et al. (2010) and its 2σ boundaries and highlight the three XCS J2215 SMGs (SMG 01, 06, and 11) that exhibit excess radio power in Figure 4. Overall, the XCS J2215 SMGs appear to have enhanced radio luminosities relative to their far-infrared emission, compared to the field population, although if we exclude the three radio-loud SMGs, the majority of the SMGs in XCS J2215 lie within the scatter of the far-infrared/radio luminosity ratios of the field SMG population.

5.2. Integrated SFR

As we have discussed, there appears to be strong evolution in the SFR of galaxies in cluster cores out to high redshift. To compare our high-redshift cluster to other low- and intermediate-redshift clusters, we therefore integrate the total SFR within the virial radius (0.8 Mpc) to obtain $\Sigma\text{SFR} = 1400^{+630}_{-440} M_{\odot} \text{yr}^{-1}$ and normalize by the cluster mass ($M_{\text{cl}} = 3 \times 10^{14} M_{\odot}$) following Popesso et al. (2012) to derive a mass-normalized SFR of $460^{+210}_{-150} / 10^{14} \text{yr}^{-1}$, shown in Figure 6. In Popesso et al. (2012), the luminosity limit ($L_{\text{IR}} \geq 10^{11} L_{\odot}$ or equivalently $\text{SFR} \geq 20 M_{\odot} \text{yr}^{-1}$) of the PACS-detected member galaxies is lower than the luminosity limit of the $850\ \mu\text{m}$ selected SMGs in XCS J2215 ($L_{\text{IR}} \geq 7 \times 10^{11} L_{\odot}$ or $\text{SFR} \geq 130 M_{\odot} \text{yr}^{-1}$). Therefore, we also calculated the mass-normalized integrated SFR including the $24\ \mu\text{m}$ sources with the limit of $\text{SFR} \geq 100 M_{\odot} \text{yr}^{-1}$ from Hilton et al. (2010) and the $[\text{O II}]$ emitters with the limit of dust-corrected $\text{SFR} \geq 10 M_{\odot} \text{yr}^{-1}$ from Hayashi et al. (2010). When including these samples in the plot, the mass-normalized integrated SFR increases by a factor of 1.5 and 2.1, respectively, compared to that determined solely from the $850\ \mu\text{m}$ selected SMGs—leading to a mass-normalized integrated SFR in galaxies with individual SFRs $\geq 10 M_{\odot} \text{yr}^{-1}$ of $(950 \pm 320) / 10^{14} M_{\odot} \text{yr}^{-1}$.

Recently, some works (e.g., Brodwin et al. 2013; Alberts et al. 2014) have argued that $z \sim 1.4$ is a critical era for star formation activity in clusters. At $z > 1.4$, the clusters selected from the IRACS Shallow Cluster Survey are dominated by

active star-forming galaxies, while at $z < 1.4$ the star formation activity in clusters is exceeded by the galaxies in less dense environments. Many studies of individual high-redshift clusters (e.g., Bayliss et al. 2014; Santos et al. 2014; Smail et al. 2014) also show enhanced star formation activities in clusters at $z > 1.4$. Smail et al. (2014) (see also Santos et al. 2014) estimated the mass-normalized star formation density ($\Sigma\text{SFR}/M_{\text{cl}}$) of a $z = 1.6$ cluster, measuring $(800 \pm 400) / 10^{14} M_{\odot} \text{yr}^{-1}$, which is consistent with the total SFR of all cluster members in XCS J2215: $(950 \pm 320) / 10^{14} M_{\odot} \text{yr}^{-1}$. Both of these clusters lie a factor $\sim 4 \times$ above the proposed rich-cluster sequence from Popesso et al. (2012) and a factor $\sim 2 \times$ above the proposed poor-cluster/group-scaling relation, suggesting that there is more star formation activity occurring in these high-redshift systems than predicted by extrapolation of these models from lower redshifts. Indeed, the mass-normalized SFRs of both of these high-redshift clusters are in better agreement with the simple $(1+z)^7$ evolution proposed by Geach et al. (2006) (see also Cowie et al. 2004).

However, as Geach et al. (2006) point out, the factor $\gtrsim 2$ scatter in mass-normalized SFR between the clusters at a fixed redshift suggests that individual cluster environments have strong influences on the star formation histories of their constituent galaxies. In particular, the enhanced star formation activities may be caused by the merging of less massive clusters or groups (as seen in merging systems at low redshift; e.g., Marcillac et al. 2007) and do not occur in more relaxed systems (e.g., a cluster at slightly lower redshift at $z = 1.39$ in Bauer et al. 2011). At present we have too few high-redshift clusters to determine whether there is similarly strong variation in levels of cluster activity to that seen at lower redshifts, or whether all high-redshift clusters display similarly levels of activity. Further deep submillimeter observations of $z \geq 1$ clusters are required to test this. However, there is already some evidence for differences between the two $z \sim 1.5$ clusters studied with SCUBA-2: the majority of the SMGs discovered in XCS J2215 lie within the core region of the cluster interspersed with the passive cluster population, whereas in CIJ0218 Smail et al. (2014) found that the cluster core was dominated by passive galaxies, with the SMGs lying on the outskirts. There are also potential differences in the apparent masses of the SMG populations in these two clusters, with Smail et al. (2014) find a median rest-frame H -band absolute magnitude (which is a crude proxy for stellar mass) for their $850\ \mu\text{m}$ detected SMGs of $M_H \sim -24.0$, compared to $M_H = -25.0 \pm 0.3$ for the SMGs in XCS J2215. The XCS J2215 SMGs are therefore brighter (and potentially more massive?) than those in CIJ0218, and so they ought to evolve into more luminous galaxies at the present day, assuming similar evolutionary pathways. Indeed, adopting a canonical burst lifetime of 100 Myr (e.g., Simpson et al. 2014), we would expect these galaxies to fade by 3.2 mag in the rest-frame H band by the present day, assuming no subsequent star formation, merging, or stripping. The median H -band absolute magnitude of the XCS J2215 SMGs would then correspond to $M_H \sim -21.8$ —the brightness of a typical elliptical galaxy at $z \sim 0$. Along with their central location, this perhaps suggests that we are seeing the final stages of the formation of the bulk of the elliptical galaxy population in XCS J2215, whereas CIJ0218, with its passive-dominated core, has already passed through this phase.

6. CONCLUSIONS

We have obtained deep 450 and 850 μm imaging of the $z = 1.46$ X-ray-selected cluster XCS J2215.9–1738 using the SCUBA-2 bolometer camera on the JCMT. We combine these new observations with multiwavelength archival data on this system, including *Spitzer* MIPS mid-infrared imaging, *Herschel* PACS far-infrared data, and VLA radio observations. Together these data provide a sensitive survey of ULIRG activity in the central regions of the cluster.

From these data we identify a significant overdensity of 11 SMGs in the cluster core. By both statistically matching these submillimeter sources to available MIPS 24 μm and 1.4 GHz radio sources and deblending the SCUBA-2 maps using the MIPS and radio catalogs as priors, we determine robust identifications of counterparts to all 11 SMGs (the majority from radio identifications).

Two of these SMG counterparts have precise spectroscopic redshifts that confirm that they are members of the cluster. Three others are identified as likely cluster members through their detection in narrowband imaging of the redshifted [O III] emission line, while a further three have photometric redshifts that are consistent with their being members. Hence, in total 8 of the 11 SMG counterparts, including all of those within the virial radius (0.8 Mpc), are probable or potential cluster members.

We fit the far-infrared and radio SEDs of the cluster members and derive typical luminosities $L_{\text{IR}} \sim (1.0 \pm 0.1) \times 10^{12} L_{\odot}$ (corresponding to an SFR = $170 \pm 20 M_{\odot} \text{yr}^{-1}$). These cluster SMGs appear to have temperatures that are $\sim 3\text{--}4$ K cooler than comparably luminous low-redshift ULIRGs, perhaps indicating a more extended distribution of dust in SMGs compared to local ULIRGs. We also show that the galaxies lie within the scatter of the radio–far-infrared correlation seen for field SMGs at high redshifts.

Finally, to investigate the evolution of the starburst population in the cores of clusters with redshift, we integrate the star formation within all galaxies in the cluster core (through our 850 μm selected SMGs, 24 μm selected galaxies, and [O III] emitters). Normalizing by the total cluster mass, we show that XCS J2215 contains one of the most active cluster cores studied to date. By combining with other low- and high-redshift samples, we show that the evolution of the mass-normalized SFR appears to continue to increase at $z \geq 1$, consistent with an evolutionary trend scaling as $(1+z)^n$ with $n \sim 7$. However, we have observations of very few clusters at $z > 1$, and so it is unclear whether the scatter between clusters that is seen in the low-redshift samples at fixed redshift (reflecting a variety of evolutionary states) also exists at high redshift. The evidence we have from the differences in the environments and near-infrared luminosities of the SMGs in the two $z \sim 1.5$ clusters studied with SCUBA-2 hints that evolutionary differences may already exist between clusters at this epoch, reflecting their different levels of development.

C.-J.M. acknowledges support from ERC Advanced Investigator programme DUSTYGAL 321334. I.R.S. acknowledges support from STFC (ST/L00075X/1), the DUSTYGAL ERC programme, and a Royal Society/Wolfson Merit Award. A.M. S. acknowledges an STFC Advanced Fellowship through grant number ST/H005234/1 and the Leverhulme Trust. The James Clerk Maxwell Telescope is operated by the Joint Astronomy Centre on behalf of the Science and Technology Facilities

Council of the United Kingdom, the National Research Council of Canada, and (until 2013 March 31) the Netherlands Organisation for Scientific Research. Additional funds for the construction of SCUBA-2 were provided by the Canada Foundation for Innovation. This work is based (in part) on observations made with the *Spitzer Space Telescope*, which is operated by the Jet Propulsion Laboratory, California Institute of Technology, under a contract with NASA. The National Radio Astronomy Observatory is a facility of the National Science Foundation operated under cooperative agreement by Associated Universities, Inc. This research has made use of NASA’s Astrophysics Data System.

REFERENCES

- Alberts, S., Pope, A., Brodwin, M., et al. 2014, *MNRAS*, 437, 437
 Barmby, P., Huang, J. S., Ashby, M. L. N., et al. 2008, *ApJS*, 177, 431
 Bauer, A. E., Grützbauch, R., Jørgensen, I., Varela, J., & Bergmann, M. 2011, *MNRAS*, 411, 2009
 Bayliss, M. B., Ashby, M. L. N., Ruel, J., et al. 2014, *ApJ*, 794, 12
 Brodwin, M., Stanford, S. A., Gonzalez, A. H., et al. 2013, *ApJ*, 779, 138
 Chapin, E., Gibb, A. G., Jenness, T., et al. 2013, *StAUN*, 258, 258
 Chapin, E. L., Hughes, D. H., & Aretxaga, I. 2009, *MNRAS*, 393, 653
 Chapman, S. C., Windhorst, R., Odewahn, S., Yan, H., & Conzelmann, C. 2003, *ApJ*, 599, 92
 Chary, R., & Elbaz, D. 2001, *ApJ*, 556, 562
 Cowie, L. L., Barger, A. J., Fomalont, E. B., & Capak, P. 2004, *ApJL*, 603, L69
 Dale, D. A., & Helou, G. 2002, *ApJ*, 576, 159
 Dawson, K. S., Aldering, G., Amanullah, R., et al. 2009, *AJ*, 138, 1271
 Downes, A. J. B., Peacock, J. A., Savage, A., & Carrie, D. R. 1986, *MNRAS*, 218, 31
 Draine, B. T., Dale, D., Bendo, G., et al. 2007, *ApJ*, 663, 866
 Dressler, A., Oemler, A., Couch, W. J., et al. 1997, *ApJ*, 490, 577
 Geach, J. E., Smail, I., Ellis, R. S., et al. 2006, *ApJ*, 649, 661
 Gómez, P. L., Nichol, R. C., Miller, C. J., et al. 2003, *ApJ*, 584, 210
 Hainline, L. J., Blain, A. W., Smail, I., et al. 2009, *ApJ*, 699, 1610
 Hainline, L. J., Blain, A. W., Smail, I., et al. 2011, *ApJ*, 740, 96
 Hayashi, M., Kodama, T., Koyama, Y., Tadaki, K.-i., & Tanaka, I. 2011, *MNRAS*, 415, 2670
 Hayashi, M., Kodama, T., Koyama, Y., et al. 2010, *MNRAS*, 402, 1980
 Hayashi, M., Kodama, T., Koyama, Y., et al. 2014, *MNRAS*, 439, 2571
 Hilton, M., Collins, C., Stanford, S. A., et al. 2007, *ApJ*, 670, 1000
 Hilton, M., Lloyd-Davies, E., Stanford, S. A., et al. 2010, *ApJ*, 718, 133
 Hilton, M., Stanford, S. A., Stott, J. P., et al. 2009, *ApJ*, 697, 436
 Hodge, J. A., Carilli, C. L., Walter, F., Daddi, E., & Riechers, D. 2013, *ApJ*, 776, 22
 Holland, W. S., Bintley, D., Chapin, E. L., et al. 2013, *MNRAS*, 430, 2513
 Ivison, R. J., Swinbank, A. M., Swinyard, B., et al. 2010, *A&A*, 518, L35
 Jenness, T., Cavanagh, B., Economou, F., & Berry, D. S. 2008, in ASP Conf. Ser. 394, *Astronomical Data Analysis Software and Systems*, ed. R. W. Argyle, P. S. Bunclark, & J. R. Lewis (San Francisco, CA: ASP), 565
 Jenness, T., Chapin, E. L., Berry, D. S., et al. 2013, *ascl soft*, 1310.007
 Karim, A., Swinbank, A. M., Hodge, J. A., et al. 2013, *MNRAS*, 432, 2
 Kennicutt, R. C. J. 1998, *ARAA*, 36, 189
 Koyama, Y., Kodama, T., Shimasaku, K., et al. 2010, *MNRAS*, 403, 1611
 Lewis, I., Balogh, M., De Propris, R., et al. 2002, *MNRAS*, 334, 673
 Lutz, D., Poglitsch, A., Altieri, B., et al. 2011, *A&A*, 532, A90
 Marcellac, D., Rigby, J. R., Rieke, G. H., & Kelly, D. M. 2007, *ApJ*, 654, 825
 Marckevitch, M. 1998, *ApJ*, 504, 27
 McMullin, J. P., Waters, B., Schiebel, D., Young, W., & Golap, K. 2007, in ASP Conf. Ser. 376, *Astronomical Data Analysis Software and Systems XVI*, ed. R. A. Shaw, F. Hill, & D. J. Bell (San Francisco, CA: ASP), 127
 Menendez-Delmestre, K., Blain, A. W., Smail, I., et al. 2009, *ApJ*, 699, 667
 Ott, S. 2010, in ASP Conf. Ser., 434, *Astronomical Data Analysis Software and Systems XIX*, ed. Y. Mizumoto, K.-I. Morita, & M. Ohishi (San Francisco, CA: ASP), 139
 Pintos-Castro, I., Sanchez-Portal, M., Cepa, J., et al. 2013, *A&A*, 558, 100
 Popesso, P., Biviano, A., Rodighiero, G., et al. 2012, *A&A*, 537, 58
 Popesso, P., Rodighiero, G., Saintonge, A., et al. 2011, *A&A*, 532, 145
 Rieke, G. H., Alonso-Herrero, A., Weiner, B. J., et al. 2009, *ApJ*, 692, 556
 Santos, J. S., Altieri, B., Popesso, P., et al. 2013, *MNRAS*, 433, 1287
 Santos, J. S., Altieri, B., Tanaka, M., et al. 2014, *MNRAS*, 438, 2565

- Santos, J. S., Altieri, B., Valtchanov, I., et al. 2015, [MNRAS](#), **447**, L65
- Simpson, J. M., Smail, I., Swinbank, A. M., et al. 2015, *ApJ*, in press (arXiv:1505.05152)
- Simpson, J. M., Swinbank, A. M., Smail, I., et al. 2014, [ApJ](#), **788**, 125
- Smail, I., Geach, J. E., Swinbank, A. M., et al. 2014, [ApJ](#), **782**, 19
- Smith, G. P., Treu, T., Ellis, R. S., Moran, S. M., & Dressler, A. 2005, [ApJ](#), **620**, 78
- Stanford, S. A., Romer, A. K., Sabirli, K., et al. 2006, [ApJL](#), **646**, L13
- Swinbank, A. M., Simpson, J. M., Smail, I., et al. 2014, [MNRAS](#), **438**, 1267
- Symeonidis, M., Vaccari, M., Berta, S., et al. 2013, [MNRAS](#), **431**, 2317
- Tadaki, K.-i, Kodama, T., Ota, K., et al. 2012, [MNRAS](#), **423**, 2617
- Thomson, A. P., Ivison, R. J., Simpson, J. M., et al. 2014, [MNRAS](#), **442**, 577
- Tran, K.-V. H., Papovich, C., Saintonge, A., et al. 2010, [ApJL](#), **719**, L126